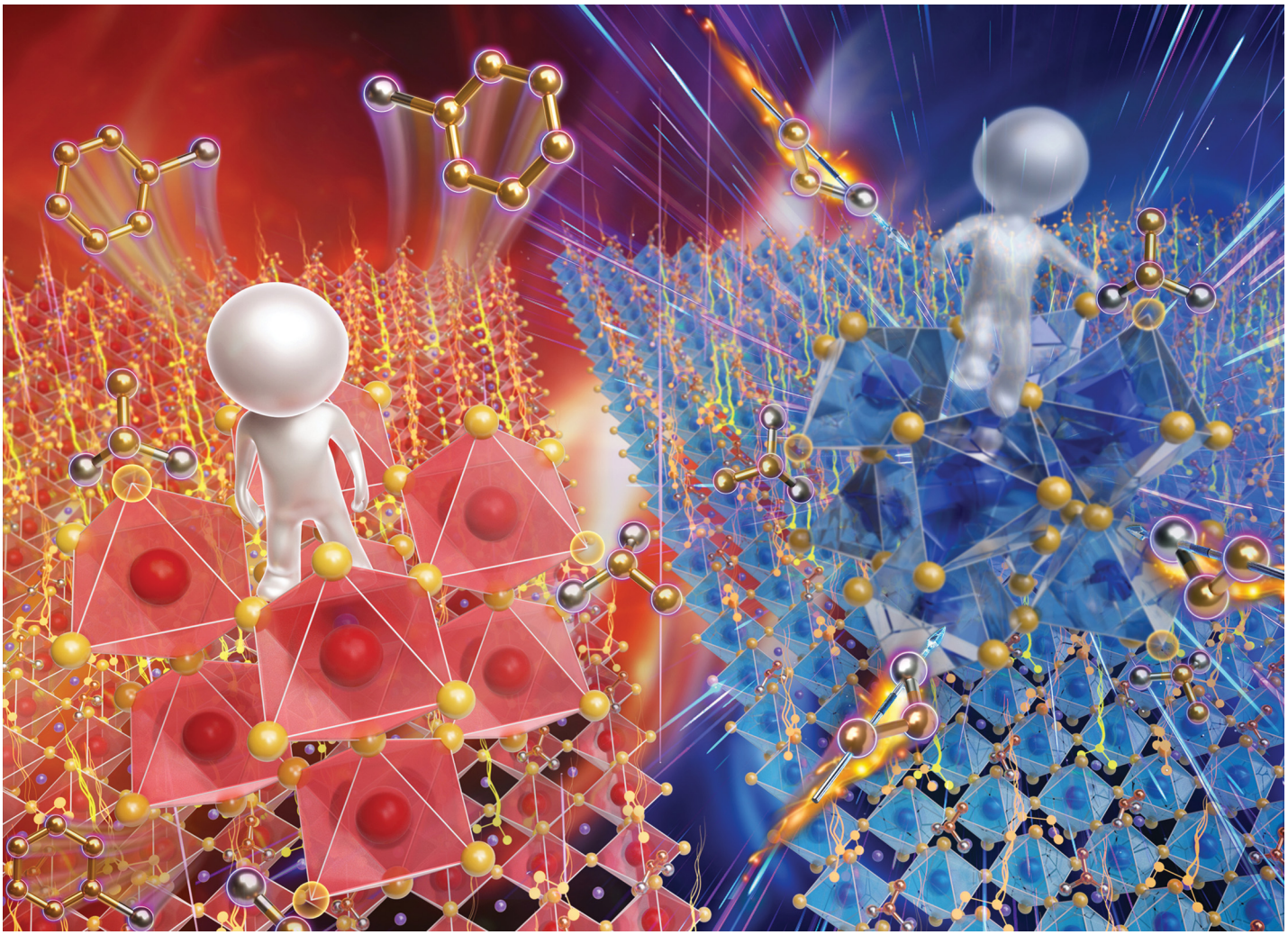


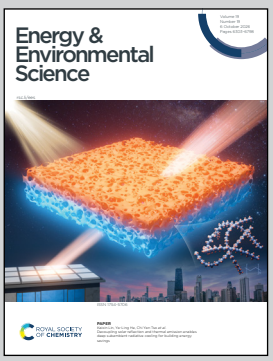
Showcasing research from Professor Meicheng Li's NEMD laboratory, School of New Energy, North China Electric Power University, Beijing, China.

Synergistic coupling enhancement and distortion suppression enable the development of 17.7%-efficient $CsPbI_3$ quantum dot solar cells

Semiconductor quantum dots offer low-temperature, eco-friendly solution processability and tunable optoelectronic properties, promising for next-generation photovoltaics. Here, an *in situ*, non-invasive capping renovation strategy is developed for $CsPbI_3$ quantum dots using a tailored phenyl acetoacetate ligand-exchange accelerator. Alkaline hydrolysis promotes efficient substitution of insulating long-chain oleates with short acetate ligands, strengthening inter-dot electronic coupling. Simultaneously, weakly adsorbing phenolic byproducts suppress lattice distortion and preserve favorable crystallographic orientation. This synergistic surface reconstruction enhances charge transport without sacrificing phase stability, enabling solar cells to achieve 17.66% record efficiency (certified 17.07%).

Image reproduced by permission of Meicheng Li from *Energy Environ. Sci.*, 2026, **19**, 6462.
Image created by Meicheng Li, Donglin Jia, and Jiaxin Li.

As featured in:



See Meicheng Li *et al.*, *Energy Environ. Sci.*, 2026, **19**, 6462.

ROYAL SOCIETY OF CHEMISTRY

rsc.li/ees

Registered charity number: 207890

Energy & Environmental Science

ROYAL SOCIETY OF CHEMISTRY

PAPER

Published on 11 August 2026
Licence and permissions

Check for updates

Cite this: *Energy Environ. Sci.*, 2026, **19**, 6462

Synergistic coupling enhancement and distortion suppression enable the development of 17.7%-efficient $CsPbI_3$ quantum dot solar cells

Donglin Jia,†[a] Jiaxin Li,†[a] Yu Han,†[ab] Meng Pang,[a] Kefan Zhu,[a] Xinchang Wang,[a] Yiran Zhao,[c] Hengwei Qiu,[a] Zhineng Lan,[a] Ruoshui Li,[a] Junjie Zhou,[a] Peng Cui,[a] Lin Zhang,[a] Ying Zhao*[b] and Meicheng Li*[a]

Received 28th April 2026,
Accepted 6th August 2026

DOI: 10.1039/d6ee02756c

rsc.li/ees

Inorganic $CsPbI_3$ perovskite quantum dots hold great promise for next-generation photovoltaics. However, competing constraints hinder postsynthetic charge transport optimization, as mild reactions inadequately remove pristine insulating ligands, whereas highly reactive conditions trigger component leaching and lattice distortion. Here we propose an *in situ* non-invasive capping renovation strategy that simultaneously regulates acyl and alkoxy segments of ester molecules. By introducing acetoacetyl moieties with doubled molar equivalents and enhanced coordination compared with conventional monoacyl groups, we achieve a 1.52-fold increase in the substitution of pristine long-chain oleate ligands with hydrolyzed short acetate species under alkaline environments without perturbing surface components, thereby effectively enhancing inter-dot electronic coupling. Meanwhile, the incorporation of phenoxy groups directs hydrolysis toward phenolic species with lower polarity and weaker adsorption than conventional alcohol byproducts, effectively suppressing orthorhombic lattice distortion of the $CsPbI_3$ framework and thus promoting a uniform face-up preferential orientation. Consequently, solar cells fabricated using phenyl acetoacetate as a ligand–exchange accelerator show suppressed trap-assisted recombination and facilitated charge extraction, achieving an efficiency of 17.66% (certified efficiency: 17.07%), the highest for inorganic quantum dot photovoltaics.

Broader context

Semiconductor quantum dots with versatile, low-temperature, and eco-friendly solution processability allow flexible tuning of their optoelectronic properties. Especially, inorganic $CsPbI_3$ perovskite quantum dots (PQDs) have attracted considerable interest for electronics, photonics, and optoelectronics due to their suitable bandgap and absence of volatile organic components. The decoupled crystallization from film deposition distinguishes them from bulk thin-film counterparts, positioning them as promising candidates for next-generation photovoltaics. However, a longstanding bottleneck hindering performance improvement of PQD solar cells (PQDSCs) lies in achieving non-destructive post-synthetic enhancement of PQD surface capping conductivity. In this work, we design an *in situ* non-invasive capping renovation strategy by integrating acetoacetyl and phenoxy moieties into a tailored ester ligand–exchange accelerator. Upon alkaline hydrolysis, pristine long-chain oleate ligands are substituted with short acetate species at a 1.52-fold higher degree than conventionally, thereby substantially strengthening inter-dot electronic coupling. Concurrently, the hydrolyzed phenolic byproducts possess low polarity and weak affinity to the PQD surface, effectively suppressing orthorhombic distortion of the $CsPbI_3$ framework. These synergistically enhance charge transport while preserving a uniform face-up crystallographic orientation. As a result, photovoltaic devices achieve champion efficiencies of 17.66% (certified efficiency: 17.07%), the highest reported for inorganic PQDSCs. By resolving the trade-off between PQD phase stabilization and charge transport optimization, this work provides a new direction for surface engineering toward high-performing solar cells and other optoelectronic devices.

1. Introduction

Perovskite quantum dots (PQDs) with versatile low-temperature solution processing and excellent optoelectronic properties show great promise in next-generation printable optoelectronic fields, such as photovoltaics,[1–3] light-emitting diodes,[4,5] and photodetectors.[6,7] Their unique colloidal nature decouples

[a] *State Key Laboratory of Alternate Electrical Power System with Renewable Energy Sources, School of New Energy, North China Electric Power University, Beijing, 102206, China. E-mail: mcli@ncepu.edu.cn*
[b] *National Institute of Clean-and-Low-Carbon Energy, Beijing Engineering Research Center of Nano-structured Thin Film Solar Cells, Beijing 102211, China. E-mail: ying.zhao.u@chnenergy.com.cn*
[c] *Zolix Analytical Instruments Co., Ltd, Beijing, 102209, China*
† Donglin Jia, Jiaxin Li, and Yu Han contributed equally.

This journal is © The Royal Society of Chemistry 2026

crystal growth from film deposition, which elegantly circumvents issues related to crystallinity and phase purity that arise from competitive nucleation of bulk counterparts, thereby enabling the large-area coating and processing of solid films *via* industrially compatible air-processing techniques.[8,9] In particular, all-inorganic $CsPbI_3$ PQDs, devoid of volatile organic components, have emerged as prominent photovoltaic candidates, benefiting from their near-ideal bandgap energy (E_g), high absorption coefficient, and high photoluminescence quantum yield (PLQY).[10–12] Guided by strategies including surface defect passivation,[11,13] surface ligand exchange,[14,15] homo/heterojunction absorber construction,[16,17] and device interfacial engineering,[16,18] the device performance of $CsPbI_3$ PQD solar cells (PQDSCs) has advanced rapidly. However, the currently available certified power conversion efficiency (PCE) of $CsPbI_3$ PQDSCs is only 13.4%, which falls far short of their ideal Shockley–Queisser limit.[19,20]

Despite its low lattice tolerance factor (0.81), the as-synthesized $CsPbI_3$ PQDs capped with long-chain oleate and oleylammonium ligands show enhanced stability of the photoactive cubic α-phase, owing to increased surface energy contribution compared to their bulk counterparts.[21,22] However, to meet the charge transport demands of photovoltaic applications, subsequent removal or exchange of these pristine insulating long-chain ligands can readily induce surface defects, lattice distortion, and even undesirable phase transitions, thereby compromising both the efficiency and stability of PQDSCs.[23] Therefore, achieving nondestructive postsynthetic enhancement of PQD surface capping conductivity is critical for advancing their performance toward practical photovoltaic deployment.

During layer-by-layer assembly of PQD light absorbers, pristine long-chain ligands can be substituted with shorter ones generated *via* ester antisolvent hydrolysis under ambient conditions.[3] Our group previously established an alkaline environment that drives this hydrolysis equilibrium forward, accelerating the formation of more target anionic species to occupy PQD surface vacancies left by pristine ligand removal, thereby improving charge transport while effectively eliminating surface defects.[24] Nevertheless, the implementation of this strategy on $CsPbI_3$ PQDs with vulnerable lattices still faces several challenges. Specifically, conventional mild ester antisolvents, such as methyl acetate (MeOAc) or ethyl acetate (EtOAc), remain insufficient for removing pristine long-chain ligands, which impedes comprehensive surface coverage by conductive ligands, thereby limiting inter-dot electron coupling.[25,26] Directly enhancing ester antisolvent polarity by introducing stronger-binding acyl groups (*e.g.*, sulfonyl, phosphoryl, and formyl) may simultaneously trigger excessively aggressive surface reactions that leach off surface halide or Pb^{2+}, inducing PQD structural collapse and film delamination.[27,28] Additionally, the yield of the target short ligands generated by ester hydrolysis is inherently constrained by the stoichiometric ratio of dissociable acyl groups in the molecule. Consequently, despite further removal of pristine ligands, the newly exposed surface coordination sites may still fail to be fully replenished.[27,29] Moreover, the potential disruptive effects of hydroxyl-containing byproducts generated from the hydrolysis of conventional aliphatic alkoxy ester antisolvents on the PQD lattice cannot be overlooked. Sun *et al.* demonstrated that polar ethanol molecules can induce lattice distortion in cubic $CsPbI_3$ nanocubes by introducing surface dipole moments, leading to self-assembly into nanowires with a 1D-orthorhombic phase.[30] Nevertheless, the impact of these *in situ* generated byproducts on the lattice structure and carrier transport of $CsPbI_3$ PQDs during ligand exchange based on ester antisolvent hydrolysis remains unexplored. As the ligand exchange progresses, their role in inducing lattice distortion may gradually become more pronounced, imposing substantial constraints on the performance and stability of PQDs and their photovoltaic devices.

In this study, we propose an *in situ* non-invasive capping renovation (NCR) strategy by simultaneously regulating acyl and alkoxy segments of ester molecules, enabling synergistic enhancement of charge transport and preservation of the cubic lattice of $CsPbI_3$ PQDs. The incorporation of acetoacetyl moieties with stronger coordination capability and doubled molar equivalents compared to conventional monoacyl increases the substitution degree by 1.52-fold of pristine long-chain oleate ligands by short acetate species generated *via* alkaline hydrolysis, without deteriorating PQD surface components, thereby substantially strengthening electronic coupling between adjacent PQDs. Meanwhile, the introduction of phenoxy groups enables esters to hydrolyze into low-polarity phenolic species. Compared with conventional alcohol byproducts that tend to disrupt the PQD lattice, they exhibit reduced adsorption affinity and wettability on the PQD surface, thereby effectively suppressing orthorhombic distortion in the $CsPbI_3$ lattice during ligand exchange and thus promoting a uniform face-up crystallographic orientation. Consequently, employing phenyl acetoacetate (PhAA) as a ligand–exchange accelerator reconstructs a conductive and well-ordered PQD surface configuration, suppressing trap-assisted recombination and facilitating efficient charge extraction. The resulting PQDSCs achieve efficiencies of 17.66% for small-area (0.07 cm^2) and 14.86% for large-area (1.00 cm^2) devices while also setting a record-high certified efficiency of 17.07% for inorganic quantum dot photovoltaics. Furthermore, the reinforced initial lattice robustness significantly improves the long-term operational stability of devices. This work provides key insights into the surface chemical engineering of PQDs and advances the practical deployment of inorganic quantum dot photovoltaics.

2. Results and discussion

2.1. Regulation of the acyl segment in ester molecules

In previous studies, low-polarity monoacyl esters, including MeOAc and EtOAc, have been widely employed to enable solid-state ligand exchange (SSLE) of $CsPbI_3$ PQDs. Although a suitable alkaline environment can accelerate their hydrolysis, the intrinsic stoichiometry restricts each ester molecule to releasing at most one target acetate ligand. As a result, such mild SSLE fails to remove a substantial fraction of the pristine

insulating ligands, while it may also leave surface vacancy defects inherited from colloidal purification (Fig. S1a). Increasing antisolvent polarity provides a direct route to ligand removal, yet highly polar esters readily induce PQD degradation.[31] In this section, we select ethyl acetoacetate (EAA) as an accelerator of the conventional SSLE process. Upon hydrolysis, each EAA molecule can generate up to two acetate anions, thereby significantly increasing the theoretical upper limit of ligand supply per ester unit. Moreover, the acetoacetate groups in EAA may promote more effective dissociation of the pristine oleate ligands from the PQD surface through stronger coordination interactions with Pb^{2+}.[32] Despite these structural merits, under conventional neutral ambient conditions, the strongly bonded acetyl moiety in EAA is difficult to cleave completely, resulting in incomplete hydrolysis and instead introducing additional vacancy defects on the PQD surface (Fig. S1b). The corresponding reaction equation is shown in eqn (1):

Neutral hydrolysis:

$$CH_3COCH_2COOC_2H_5 + H_2O \rightarrow CH_3COCH_2COOH + C_2H_5OH \quad (1)$$

Building on our previous work, potassium hydroxide (KOH) was introduced to create an alkaline environment that drives the complete hydrolysis of EAA (Fig. S1c). The corresponding reaction equation is shown in eqn (2):

Alkaline hydrolysis:

$$CH_3COCH_2COOC_2H_5 + 2OH^- \rightarrow 2CH_3COO^- + C_2H_5OH \quad (2)$$

Therefore, as illustrated in Fig. 1a, compared with conventional ester antisolvents (*e.g.*, EtOAc), EAA is expected to more effectively facilitate the substitution of pristine long-chain ligands with shorter ones derived from its hydrolysis under alkaline environments, thereby substantially enhancing electronic coupling between adjacent PQDs.

$CsPbI_3$ PQD colloids capped with pristine oleate and oleylammonium ligands were synthesized *via* a modified hot injection method and purified twice. The resulting products were monodispersed with a statistical particle size of 12.4 ± 1.2 nm (Fig. S2). The as-synthesized colloids were deposited into solid films, named "pristine", which were subsequently

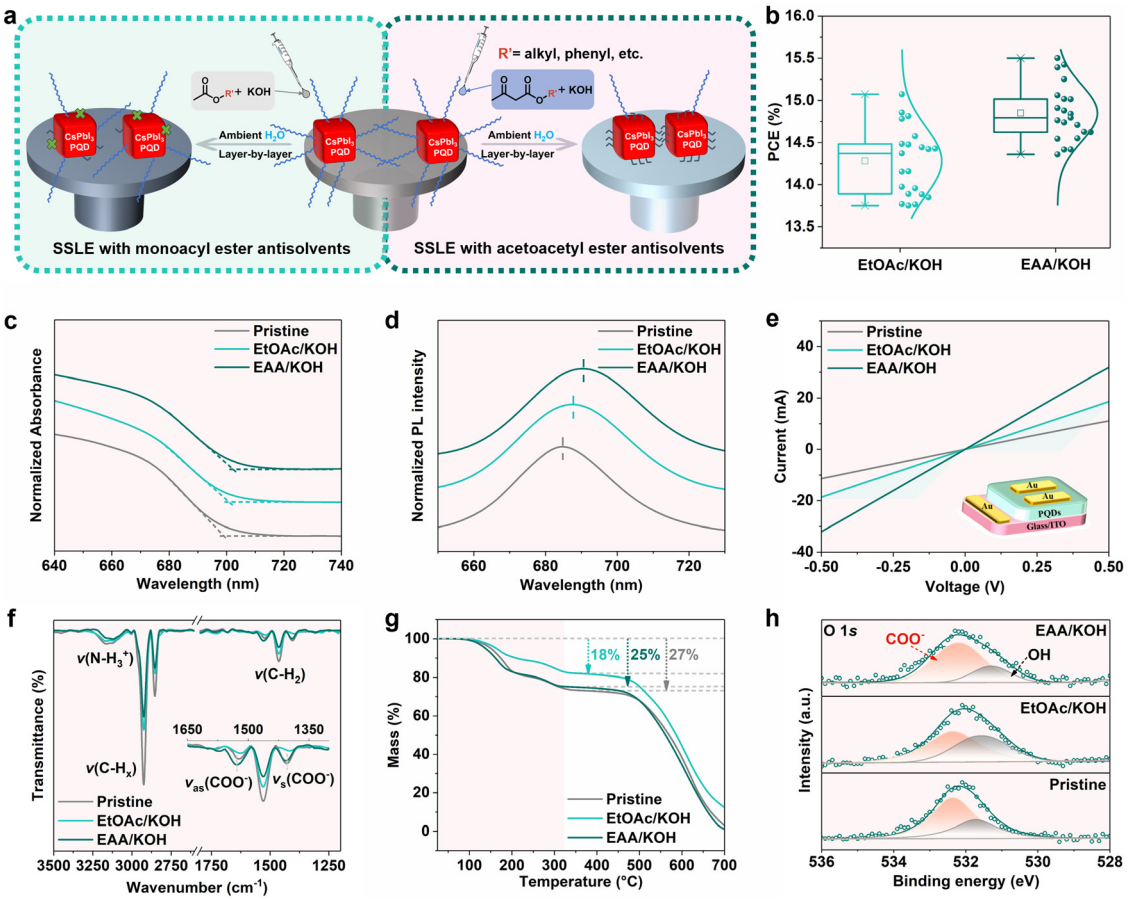


Fig. 1 Effects of acyl moieties in ester molecules on surface chemistry of $CsPbI_3$ PQDs. (a) Schematic illustration of solid-state ligand exchange of PQDs using ester antisolvents with different acyl moieties. (b) Statistical distribution of PCE for EtOAc/KOH- and EAA/KOH-based PQDSCs. For each condition, 21 devices fabricated from different batches were included in the statistical analysis. (c)–(h) Normalized light absorption spectra (c), normalized PL spectra (d), vertical conductivity (e), FT-IR spectra (f), TGA curves (g) and O 1s core level XPS spectra (h) of pristine, EtOAc/KOH-based, and EAA/KOH-based PQDs.

 This journal is © The Royal Society of Chemistry 2026

subjected to the SSLE process *via* rinsing with saturated KOH solutions of ester antisolvents (denoted as ester/KOH) under ambient conditions with a relative humidity (RH) of 20–30%. Considering that the highly polar methanol generated from MeOAc hydrolysis under alkaline conditions may introduce drastic local reactions to the PQD surface, thereby lowering the processing reproducibility, EtOAc was selected as the benchmark ester antisolvent in this work. Samples rinsed with conventional EtOAc/KOH were used as the control. For samples prepared with the EAA accelerator, given its high polarity (dielectric constant, ε = 15 *vs.* 6.02; EAA *vs.* EtOAc), we formulated an optimized antisolvent by mixing EAA with EtOAc at a volume ratio of 1 : 9 ($\varepsilon \approx 7$). This blended antisolvent delivered superior performance for both PQD solids and solar cells (Fig. S3 and Table S1), which is hereafter referred to simply as ''EAA''. In addition, we explored esters bearing other strongly polar functional groups (*e.g.*, sulfonyl and phosphoryl) as alternative accelerators (Fig. S4). While their low-level incorporation (<10%) into EtOAc does not cause overt PQD degradation, the anionic species derived from their alkaline hydrolysis formed excessively strong coordination interactions with the $CsPbI_3$ lattice compared to carboxyl groups, leading to substantial Pb and I leaching from PQDs, as evidenced by inductively coupled plasma mass spectrometry (ICP-MS).[33,34] This process deteriorates the optoelectronic properties of PQD solids, unfavorable to photovoltaic device fabrication. In contrast, EAA effectively circumvents these adverse effects, exhibiting superior potential for surface chemical regulation.

We first evaluated the influence of the acyl moiety of ester antisolvents on the photovoltaic performance of PQDs by fabricating solar cell devices. During the layer-by-layer deposition of the PQD light absorber, only the alternative ester antisolvents were used for interlayer rinsing, without additional post-treatment. Fig. 1b and Fig. S5 present the statistical distributions of PCE and other photovoltaic parameters, with the corresponding statistical data summarized in Table S2. Compared with EtOAc/KOH-based PQDSCs showing a statistical (champion) PCE of 14.28% (15.08%), EAA/KOH-based devices demonstrate an enhanced average (champion) efficiency of 14.85% (15.51%).

To clarify the mechanism underlying the improved device performance, we conducted comprehensive characterization on PQDs. Fig. 1c and d present the normalized light absorption and PL spectra of PQD solids, respectively. The pristine PQDs without antisolvent rinsing exhibit a PL emission centered at 684 nm. Notably, rinsing with EAA/KOH induced a more pronounced red shift in both light absorption and PL emission compared to the EtOAc/KOH treatment (689 nm *vs.* 687 nm; EAA/KOH *vs.* EtOAc/KOH). This spectral shift, together with the reduced interparticle spacing and nearly invariant PQD sizes revealed by high-angle annular dark-field (HAADF) analysis (Fig. S6), indicates enhanced electronic coupling between adjacent PQDs upon EAA/KOH rinsing.[35] As a result, EAA/KOH more effectively improves charge transport and electrical conductivity in PQD solids than the conventional EtOAc/KOH treatment (Fig. 1e). Upon accounting for the film thickness determined by scanning electron microscopy (SEM, Fig. S7), the vertical conductivity of EAA/KOH-based PQD solids is calculated to be 1.6-fold higher than that of the EtOAc/KOH counterparts.

Fourier-transform infrared (FT-IR) spectroscopy was employed to probe the surface chemistry of $CsPbI_3$ PQDs, revealing that ester antisolvent rinsing markedly suppresses the alkyl (1460 and 2920 cm^{-1}) and ammonium (3100–3300 cm^{-1}) vibrations of the pristine PQDs (Fig. 1f). Notably, compared with the EtOAc/KOH counterpart, EAA/KOH-based PQDs exhibit intensified carboxyl stretching modes ($\upsilon(COO^-)$) at 1408 and 1530 cm^{-1}, with intensities even exceeding those of the pristine sample. As a result, the weakest CH_2 and the strongest COO^- signals in EAA/KOH-based PQDs suggest extensive substitution of pristine long-chain oleate ligands by short acetate species. Quantitative characterization further corroborated these findings. Thermogravimetric analysis (TGA) curves (Fig. 1g) show that the sublimation of organic species on the PQD surface occurs before 320 °C, whereas thermal decomposition of the $CsPbI_3$ perovskite core proceeds above 550 °C. Derivative thermogravimetric (DTG) curves further reveal lower sublimation temperatures for organic species in ester antisolvent-rinsed PQDs, consistent with the volatilization of short ligands without extensive hydrocarbon-chain decomposition (Fig. S8a). Notably, the weight of organic ligands in EAA/KOH-based PQDs reaches 25%, markedly exceeding that of EtOAc/KOH counterparts (18%), and approaching pristine levels (27%). Combined with FT-IR evidence, this confirms that the increased TGA mass loss originates primarily from enhanced short acetate ligand coverage on the PQD surface, formed upon alkaline hydrolysis of EAA. To better quantify the extent of ligand exchange, we performed an integration analysis of the peak area at ~5.3 ppm in the ^1H nuclear magnetic resonance (NMR) spectra (Fig. S8b), which represents the amount of the oleyl species. The results demonstrate that EAA/KOH enables approximately 1.52-fold greater substitution of pristine long-chain oleate ligands by short acetate species compared to conventional EtOAc/KOH rinsing. X-ray photoelectron spectroscopy (XPS) analysis confirms that antisolvent rinsing with either EtOAc/KOH or EAA/KOH does not affect the inorganic $CsPbI_3$ framework of PQDs (Fig. S9 and Table S3), consistent with ICP-MS results. Notably, as shown in Fig. 1g, the intensity ratio between carboxyl (~532.5 eV) and hydroxyl (~531.4 eV) for EAA/KOH-based PQDs (2.81) is substantially higher than that for the EtOAc/KOH counterpart (1.28), with a ratio even higher than that of the pristine PQDs (2.13). Considering the essentially unchanged iodine content before and after antisolvent rinsing, these results indicate that EAA/KOH treatment effectively compensates surface anionic vacancies generated upon the desorption of pristine oleate ligands, including those inherited from colloidal purification, through the coordination of hydrolyzed short acetate ligands, thereby enabling the formation of conductive PQD matrices covered with a higher density of short ligands.

2.2. Optimization of the alkoxy segment in ester molecules

Although the EAA/KOH antisolvent system effectively facilitates inter-dot electronic coupling while simultaneously mitigating

surface defects, the assembled light absorbers do not exhibit the anticipated substantial improvements in optoelectronic and photovoltaic performance compared with their EtOAc/KOH counterparts. Therefore, it is imperative to further elucidate the influence of ester antisolvents on other surface characteristics of $CsPbI_3$ PQDs to achieve comprehensive optimization. Besides anionic products derived from the acyl moiety of esters, the effects of hydroxyl-containing byproducts generated from their alkoxy moiety on PQD structural integrity and device performance have remained largely unexplored, particularly under conditions of increased ester hydrolysis degree.[36] Compared with the conventional aliphatic alcohol byproducts (ethanol or methanol), phenol with aromatic tail-groups exhibits distinct physicochemical attributes: (i) lower dielectric constant (15 *vs.* 24.3; phenol *vs.* ethanol), thereby introducing minimal additional dipolar perturbation at the PQD surface. (ii) Lower saturated vapor pressure (0.047 kPa *vs.* 7.87 kPa; phenol *vs.* ethanol), conferring attenuated molecular mobility and diffusion kinetics under ambient conditions. (iii) Conjugated π-electron character, leading to weaker coordination toward Pb^{2+} in the PQD lattice.[37] Therefore, ester antisolvents featuring aromatic alkoxy groups are promising to mitigate lattice erosion and structural disruption in $CsPbI_3$ PQDs, thereby further enhancing device performance.

Accordingly, PhAA, incorporating both phenoxy and acetoacetyl functionalities, was developed as an alternative SSLE accelerator. Upon blending it with phenyl acetate (PhOAc, ε = 6.88) and introducing the mixture into the KOH environment, the PhAA/KOH antisolvent was established. Density functional theory (DFT) calculations were first performed to elucidate the feasibility of PhAA as an accelerator for SSLE by identifying transition states (TS) associated with its alkaline hydrolysis, as depicted in Fig. 2a. The initial adsorption of PhAA onto hydroxyl groups to form tetrahedral intermediate 1 (process I, −1.6 eV) and the subsequent hydrogen rearrangement in intermediate 2 to yield the final products (process III, −4.0 eV) are both highly exergonic. By contrast, the tetrahedral decomposition (ester bond heterolysis) from intermediate 1 to 2 (process II) requires only modest activation energy to surmount the TS barrier (1.0 eV). Collectively, these results demonstrate that the alkaline hydrolysis of PhAA at PQD surfaces is thermodynamically favorable and kinetically accessible under ambient conditions.

Following this, we rinsed the $CsPbI_3$ PQD films using PhAA/KOH and subsequently compared their properties against samples analyzed in the preceding section. Fig. S10 reveals that the pristine long-chain oleate ligands on the PQD surface are effectively substituted by short acetate ligands only upon rinsing with PhAA/KOH instead of the KOH solution of neat PhOAc. Notably, the shift of $\upsilon(COO^-)$ from 1530 cm^{-1} for the EAA/KOH-based sample to 1565 cm^{-1} for the PhAA/KOH-based PQDs indicates strengthened coordination of acetate ligands to PQD surfaces. Optoelectronic characterization reveals that PhAA/KOH-based PQDs exhibit an identical emission peak position to their EAA/KOH counterparts while exhibiting enhanced PL intensities with reduced full width at half maximum (FWHM) compared to both EAA/KOH- and EtOAc/KOH-based samples (Fig. S11a). TRPL measurements further corroborate the emission improvement, revealing a prolonged average carrier lifetime of 5.86 ns for PhAA/KOH-based PQDs, as compared to 4.86 ns and 4.10 ns for EAA/KOH and EtOAc/KOH counterparts, respectively (Fig. S11b and Table S4). These combined results indicate that the mechanism by which PhAA/KOH suppresses nonradiative recombination in PQD solids extends beyond ligand exchange and surface defect passivation. We therefore systematically investigated their

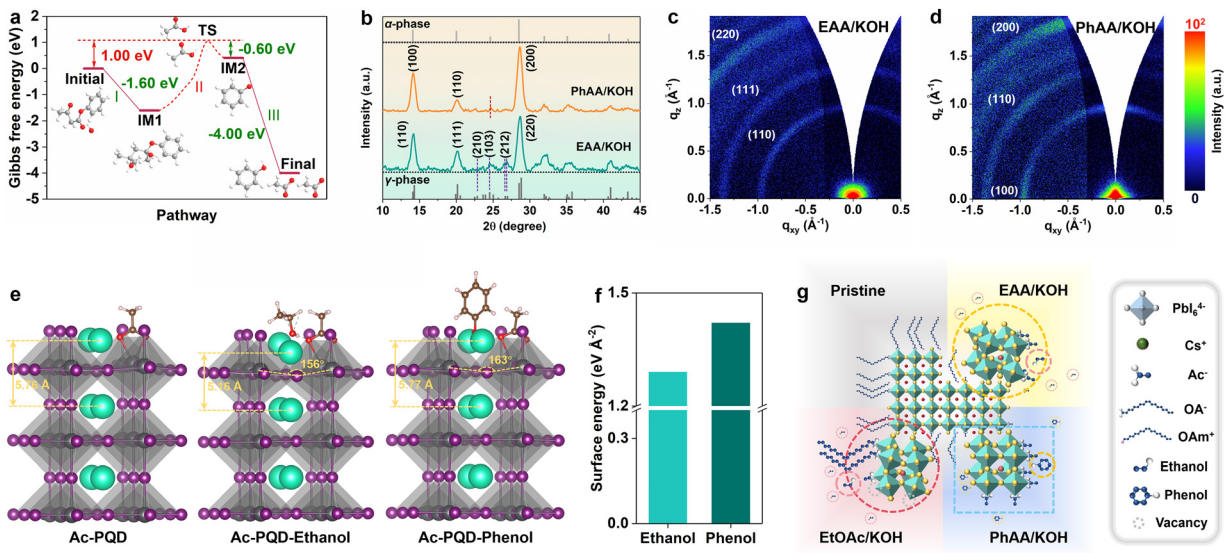


Fig. 2 Effects of alkoxy moieties in ester molecules on crystal structures of $CsPbI_3$ PQDs. (a) Calculated ΔG variations for PhAA hydrolysis under alkaline conditions. (b) XRD patterns of EAA/KOH- and PhAA/KOH-based PQDs. (c) and (d) 2D GIWAXS patterns of EAA/KOH-based (c) and PhAA/KOH-based (d) PQD solids. (e) and (f) DFT-calculated surface structure (e) and corresponding surface energy (f) of acetate-capped $CsPbI_3$ (001) slabs adsorbed with an ethanol or phenol molecule. (g) Schematic illustration of PQD lattice evolution during SSLE using different ester antisolvents.

 This journal is © The Royal Society of Chemistry 2026

structural characteristics (Fig. 2b and Fig. S12a). X-ray diffraction (XRD) analysis reveals that both EtOAc/KOH- and EAA/KOH-based PQDs exhibit pronounced γ-phase $CsPbI_3$ patterns, indicative of orthorhombic lattice distortion. In contrast, the PhAA/KOH-based sample largely preserves the ordered α-phase features of the pristine state and exhibits a smaller (110)/(200) peak area ratio compared to the EAA/KOH counterpart (0.176 *vs.* 0.393; PhAA/KOH *vs.* EAA/KOH), likely indicating preferential orientations. Moreover, EAA was also introduced into PhOAc/KOH for solid-state rinsing. In contrast to the overall preserved α-phase pattern retained after neat PhOAc/KOH rinsing, the addition of EAA into PhOAc/KOH induces pronounced γ-phase features in PQDs, similar to those observed in the EAA/KOH-based sample (Fig. S12b), highlighting the dominant role of ligand–exchange accelerators in governing PQD structural evolution rather than carrier antisolvents.

Grazing-incidence wide-angle X-ray scattering (GIWAXS) was further employed to systematically investigate the crystallographic characteristics of EAA/KOH- and PhAA/KOH-based PQDs assembled on substrates (Fig. 2c). Both samples exhibit scattering rings corresponding to the crystallographic planes identified by XRD. However, compared with the EAA/KOH counterparts, PhAA/KOH-based PQDs display more pronounced intensity arcs superimposed on these rings, indicative of preferential orientations. To quantitatively assess this disparity, azimuthal integration analysis of the first scattering ring was conducted (Fig. S13). The PhAA/KOH-based PQD assembly demonstrates substantially enhanced integrated scattering intensity at 90°, confirming a well-defined face-up $(001)||_S$ orientation on the substrate. In contrast, the EAA/KOH counterpart shows weaker and broader features at azimuthal angles of 45° and 135°, corresponding to an obscured corner-up $(111)||_S$ orientation, which can be attributed to the tilting distortion of the $[PbI_6]^{4-}$ octahedra.[38] Moreover, atomic force microscopy (AFM) imaging (Fig. S14) reveals a substantially lower root-mean-square roughness of the PhAA/KOH-based PQD solid (S_q = 2.5 nm) compared to the EAA/KOH counterparts (S_q = 3.6 nm). These morphological observations corroborate the improved crystallographic orientations determined from GIWAXS measurements.

Since PhAA and EAA share the same acetoacetate moiety, the superior performance of PhAA-treated PQDs is likely derived from their alkoxy group. To clarify this effect, an in-depth study was carried out by further employing DFT calculations to probe the atomic-scale structural response of $CsPbI_3$ PQDs to the adsorption of byproducts generated from ester antisolvent hydrolysis. As illustrated in Fig. 2e, a CsI-terminated $CsPbI_3$ (001) surface slab was constructed, in which one surface iodide was substituted by an acetate ligand to represent realistic surface chemistry. This model is referred to as Ac-PQD (model I). Upon adsorption of ethanol with a large dipole moment (μ = 1.67 D, Fig. S15), pronounced distortions are introduced in the $CsPbI_3$ PQD surface lattice (named Ac-PQD-ethanol, model II). Specifically, strong hydrogen-bonding interactions between the hydroxyl group and surface iodide ions disrupt the local lattice symmetry, resulting in noticeable displacement of Cs atoms from their equilibrium lattice positions and a substantial contraction of surface Pb–I–Pb bond angles. In contrast, the adsorption of phenol largely preserves the structural regularity of the pristine Ac-PQD surface lattice (denoted as Ac-PQD-Phenol, model III). This behavior can be attributed to its lower polarity (μ = 1.33 D) together with steric constraints imposed by the aromatic ring. Thermodynamic analysis further highlights the distinct interactions of hydrolyzed byproducts with PQD surfaces. Surface energy calculations show that the Ac-PQD-Phenol surface exhibits a higher value of 1.42 eV $Å^{-2}$, in contrast to 1.29 eV $Å^{-2}$ for the Ac-PQD-Ethanol surface (Fig. 2f). This result reveals that phenol is less favorable for adsorption to the $CsPbI_3$ PQD surface, therefore inducing a substantially weaker lattice perturbation.

To experimentally assess the impact of ester hydrolysis byproducts on the $CsPbI_3$ PQD lattice, we monitored the dynamic wetting behavior of droplets comprising 1 M ethanol in EtOAc (EtOH/EtOAc) *versus* 1 M phenol in PhOAc (PhOH/PhOAc) on PQD solids. The phenol/PhOAc droplet shows a contact angle of approximately 60° on the PQD solid, far exceeding the values below 5° observed for ethanol/EtOAc droplets, which reflects substantially weaker wettability, thus leading to reduced spreading on the PQD surface. (Fig. S16). The rinsing-time-dependent evolution of PQD solid morphology further confirms that the phenol/PhOAc solution is more readily removed during the spin-coating/rinsing process, which prevents excessive infiltration into the PQD film, thereby averting potential lattice invasion (Fig. S17a). XRD analysis revealed distinct structural evolution pathways of the PQD lattice (Fig. S17b). For the EtOH/EtOAc-treated sample, the (110) reflection was markedly suppressed, accompanied by the sharpening of the (100) and (200) peaks and their shift toward higher diffraction angles. According to the Scherrer equation, the reduced FWHM of these reflections corresponds to an increase in particle size, indicating that ethanol adsorption triggers rapid lattice distortion of PQDs, thereby inducing their oriented self-assembly. In contrast, PQDs treated with PhOH/PhOAc largely retained the structural features of photoactive black-phase nanocubes, indicating substantially alleviated lattice perturbation. Therefore, both the theoretical and experimental results demonstrate that the further enhanced optoelectronic performance of $CsPbI_3$ PQDs achieved using PhAA as the antisolvent arises from its favorable phenol byproducts, which effectively suppress lattice distortion.

Based on the above results, the mechanism of our *in situ* NCR strategy is summarized in Fig. 2g. This protocol synergistically integrates ligand regulation and lattice stabilization. Conventional mild SSLE based on the pure EtOAc antisolvent not only inefficiently strips pristine long-chain ligands but also risks inducing lattice distortion. To overcome these limitations, acetoacetyl functionality with doubled molar equivalents and enhanced coordination strength is introduced under alkaline conditions, enabling more complete substitution of pristine insulating oleate ligands by conductive acetate species, thereby strengthening inter-dot electronic coupling and suppressing surface defects without inducing compositional leaching.

Moving forward, optimization of the alkoxy functionality identifies PhAA as the preferred accelerator for the SSLE process, whose hydrolysis generates phenolic byproducts with reduced affinity and erosivity toward the PQD lattice compared to conventional alcohols. As a result, PhAA enables a more efficient ligand exchange while preserving the cubic lattice integrity of $CsPbI_3$ PQDs, thereby reconstructing a conductive and well-ordered surface configuration.

2.3. Photovoltaic performance of solar cells

To study the effect of the *in situ* NCR strategy on the photovoltaic performance of PQDs, we fabricated solar cells with n–i–p structure indium-doped tin oxide (ITO)/tin dioxide (SnO_2)/PQDs/2,2′,7,7′-tetrakis[*N*,*N*-bis(4-methoxyphenyl)amino]-9,9′-spirobifluorene (Spiro-OMeTAD)/Au (Fig. 3a). Light absorbers were fabricated *via* layer-by-layer assembly using a moderate PQD concentration (85 mg mL^{-1}) to ensure efficient interlayer ligand exchange. Gradual build-up was achieved through 3–5 sequential deposition/ligand–exchange cycles, followed by benzamidinium ($PhAD^+$) post-treatment to substitute the pristine long-chain oleylammonium ligands on PQD A-sites, thereby further optimizing charge transport.[24] This process yielded absorbers with thicknesses of up to ~620 nm. As surface chemistry contributes to governing the band energetics of PQDs, ultraviolet photoelectron spectroscopy (UPS) was performed to determine their electronic structures (Fig. S18). PhAA/KOH-based PQDs show downshifted energy levels compared to their EAA/KOH counterparts, favorable for efficient electron and hole extraction (Fig. 3b).[39]

Solar cell performance was evaluated under AM1.5G illumination (100 mW cm^{-2}). As shown in the photocurrent density–voltage (*J*–*V*) curves of the best-performing devices (Fig. 3c), EAA/KOH-based PQDSCs exhibit a maximum PCE of 16.06%, with an open-circuit voltage (V_{OC}) of 1.23 V, a short-circuit current density (J_{SC}) of 17.67 mA cm^{-2}, and a fill factor (FF) of 0.739. In contrast, PhAA/KOH-based PQDSCs deliver significantly enhanced device performance, achieving a champion PCE of 17.66%, accompanied by a V_{OC} of 1.26 V, a J_{SC} of 17.80 mA cm^{-2}, and an FF of 0.778 upon optimization of the PhAA content in EtOAc/KOH (Fig. S19a and Table S5). Notably, these champion metrics were obtained from an optimized 4-layer PQD absorber (Fig. S19b). Notably, the best-performing

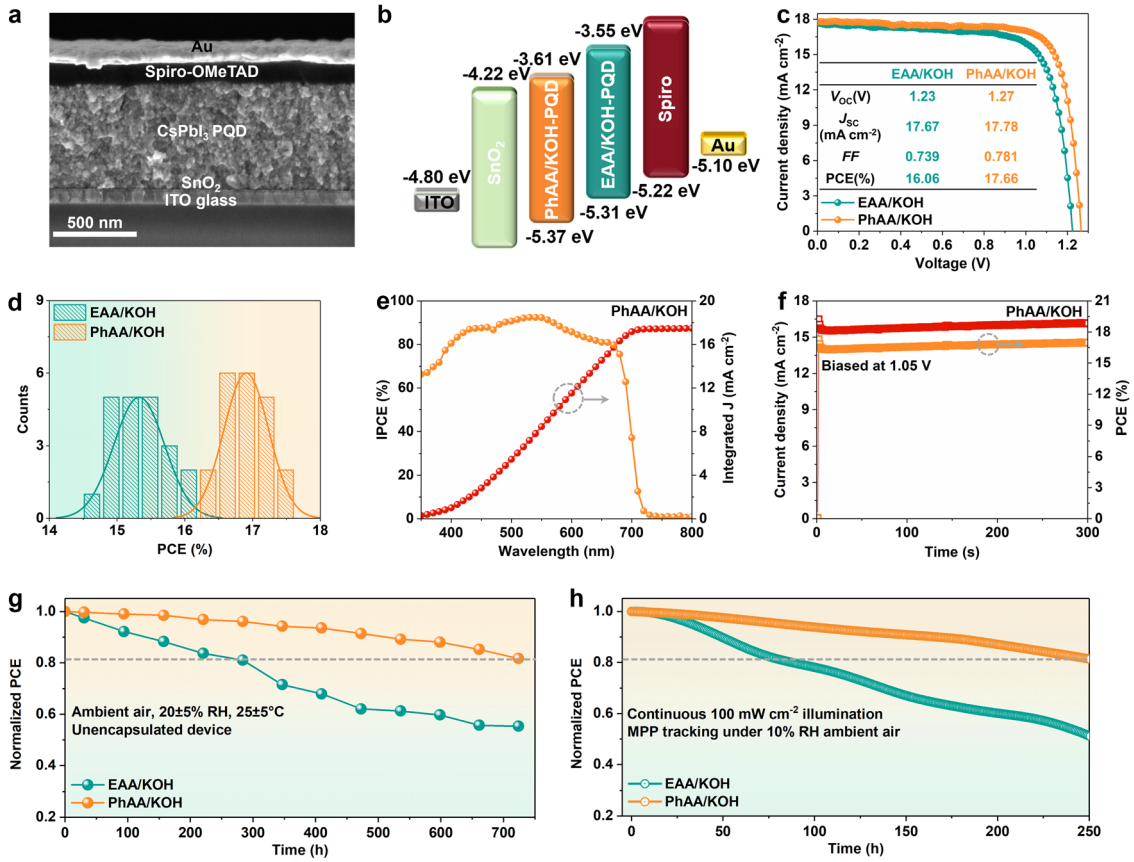


Fig. 3 Effects of the *in situ* NCR strategy on photovoltaic performance of PQDSCs. (a) Cross-sectional SEM image of the $CsPbI_3$ PQDSC device. (b) Energy level diagram of functional layers in EAA/KOH- and PhAA/KOH-based PQDSCs, with band positions of carrier transport layers obtained from the literature. (c) and (d) champion *J*–*V* curves and (c) statistical PCEs (d) of EAA/KOH- and PhAA/KOH-based PQDSCs. For each condition, 21 devices fabricated from different batches were included in the statistical analysis. (e) and (f) IPCE spectrum (e) and stabilized PCE (f) of the PhAA/KOH-based PQDSC. (g) and (h) Stability of unencapsulated EAA/KOH- and PhAA/KOH-based PQDSCs under ambient conditions of 25 ± 5% RH storage (g), and continuous 100 mW cm^{-2} white LED illumination in ambient air with a RH of 10% (h).

 This journal is © The Royal Society of Chemistry 2026

PhAA/KOH-based PQDSC was certified by an independent solar cell accreditation laboratory, demonstrating a PCE of 17.07% (Fig. S20), marking the highest certified value among inorganic quantum dot solar cell (QDSC) reports to date, as summarized in Table S6. Despite slight hysteresis being observed when recording *J–V* curves under different voltage scanning directions, a common phenomenon for solar cells with highly doped Spiro-OMeTAD as the hole-transport material, it was substantially mitigated in PhAA/KOH PQDSCs compared to the EAA/KOH counterparts (Fig. S21).[40,41]

Photovoltaic parameter statistics of devices further confirm the performance enhancement (Fig. 3d and Fig. S22 and Table S7). The PhAA/KOH-based PQDSCs showed a higher average PCE of 16.77% compared to 15.33% for the EAA/KOH counterparts, primarily due to the improved statistical V_{OC} and FF values. The incident photon-to-electron conversion efficiency (IPCE) spectra (Fig. 3e) yield an integrated current density of 17.52 mA cm^{-2} for PhAA/KOH-based devices, in good agreement with the J_{SC} derived from the champion *J–V* curve ($\sim$1.46% discrepancy), confirming the reliability of the device performance evaluation. Consistently, the stabilized power output (SPO) efficiency of PhAA/KOH-based devices reaches 17.00% (Fig. 3g), matching their PCE values extracted from *J–V* curves. To assess the scalability of the *in situ* NCR strategy, we fabricated 1 cm^2 solar cells (Fig. S23). The champion device delivered a PCE of 14.86%, the highest reported for large-area ($\geq$1 cm^2) inorganic PQDSCs.

Device stability is another critical metric for evaluating the overall performance of $CsPbI_3$ PQDSCs. Due to the size mismatch between small Cs^+ (167 pm) and large I^- (220 pm), the lattice structure of the $CsPbI_3$ perovskite is intrinsically fragile (tolerance factor: 0.81). This vulnerability is pronounced in antisolvent-rinsed solids, where the initial lattice strain renders PQDs susceptible to transformation into the thermodynamically more stable one-dimensional δ phase during storage or operation.[42] Therefore, we first assessed the ambient storage stability of $PhAD^+$ post-treated $CsPbI_3$ PQD light absorbers under 30 $\pm$ 5% relative humidity (RH). As shown in Fig. S24, EAA/KOH-based PQDs degraded rapidly, with almost complete conversion to the δ phase within 20 days of storage. In contrast, the PhAA/KOH-based PQD absorber exhibited substantially enhanced storage stability, showing negligible degradation after an identical aging process. This improvement is likely attributable to the suppression of the unfavorable PbI_6 octahedral tilting in the as-prepared state.

Subsequently, we examined the shelf life of unencapsulated PQDSCs. As shown in Fig. 3g, the EAA/KOH-based devices lost $\sim$60% of their initial efficiency after 30 days of storage under ambient conditions (10–20% RH), whereas the PhAA/KOH-based devices retained $\sim$80% over the same aging period. We further assessed the operational stability by tracking the maximum power point under continuous 100 mW cm^{-2} white light illumination under 10% RH ambient conditions (Fig. 3h). The PhAA/KOH-based PQDSCs maintained $\sim$80% of their initial efficiency after 250 h of aging, while the EAA/KOH counterparts retained only $\sim$50%. As a result, the markedly improved stability of PhAA/KOH-based PQDSCs is attributed to the *in situ* shielding effect afforded by the PhAA antisolvent to the PQD lattice, which enhances structural tolerance against environmental and continuous light stress.

2.4. Charge carrier collection and recombination in PQDSCs

To gain deeper insight into the mechanisms by which the *in situ* NCR strategy enhances the photovoltaic performance of solar cells, we systematically analyzed the carrier dynamics in PQD light absorbers prepared *via* $PhAD^+$ ligand post-treatment. XRD and FT-IR analyses confirmed that $PhAD^+$ effectively substituted the pristine long-chain oleylammonium ligands at surface A-sites, thereby facilitating charge transport without altering the PQD crystal structure or disrupting the carboxylate coordination established during the preceding interlayer ligand exchange (Fig. S25). Fig. 4a and b present 2D pseudo-color PL intensity maps of monolayer PQD absorbers. The PhAA/KOH-based sample exhibits a more uniform emission distribution than the EAA/KOH counterpart, which likely reflects reduced nanocrystal aggregation. Such aggregation in the EAA/KOH sample is plausibly induced by the polarization effect of ethanol byproducts on the PQD surface. Consistent with this observation, SEM images show that the PhAA/KOH-based PQD absorber possesses a smoother surface with more homogeneous PQD stacking than the EAA/KOH counterpart (Fig. S26). Fig. 4c and d show the weighted-average fluorescence lifetime maps of the PQD absorber, obtained by fitting the decay profiles with a biexponential function. The corresponding lifetime components are presented in Fig. S27, with fitting parameters summarized in Table S8. The PhAA/KOH-based sample exhibits consistently longer average carrier lifetimes across the mapped region compared with the EAA/KOH counterpart. Moreover, its fast decay component shows a more homogeneous spatial lifetime distribution with substantially fewer low-lifetime domains. These findings demonstrate that PhAA/KOH interlayer rinsing non-invasively suppresses nonradiative recombination through the entire PQD solid, rather than *via* a localized effect.[43,44]

To further quantify carrier trapping and transport in the PQD absorbers, electron-only devices with the structure ITO/SnO_2/PQDs/PCBM/Ag were fabricated for space-charge-limited current (SCLC) analysis. The dark current–voltage (*I–V*) curves are shown in Fig. 4e. The trap density (N_{trap}) was calculated using eqn (3):

$$N_{trap} = \frac{2\varepsilon_0\varepsilon_r V_{TFL}}{eL^2} \quad (3)$$

where V_{TFL} is the trap-filled limit voltage, L is the thickness of PQD absorbers, and ε_0 and ε_r are the vacuum permittivity and relative dielectric constant of $CsPbI_3$ PQDs, respectively. The calculated N_{trap} value for PhAA/KOH-based devices is 3.1 $\times$ 10^{14} cm^{-3}, lower than 4.8 $\times$ 10^{14} cm^{-3} for their EAA/KOH counterparts. Moreover, the electron mobility (μ_e) of PQD absorbers was calculated using the Mott–Gurney equation:[45]

$$\mu_e = \frac{8J_D L^3}{9\varepsilon_0\varepsilon_r V^2} \quad (4)$$

where J_D is the dark current density in the SCLC region, and V is the applied voltage. Compared with EAA/KOH-based devices,

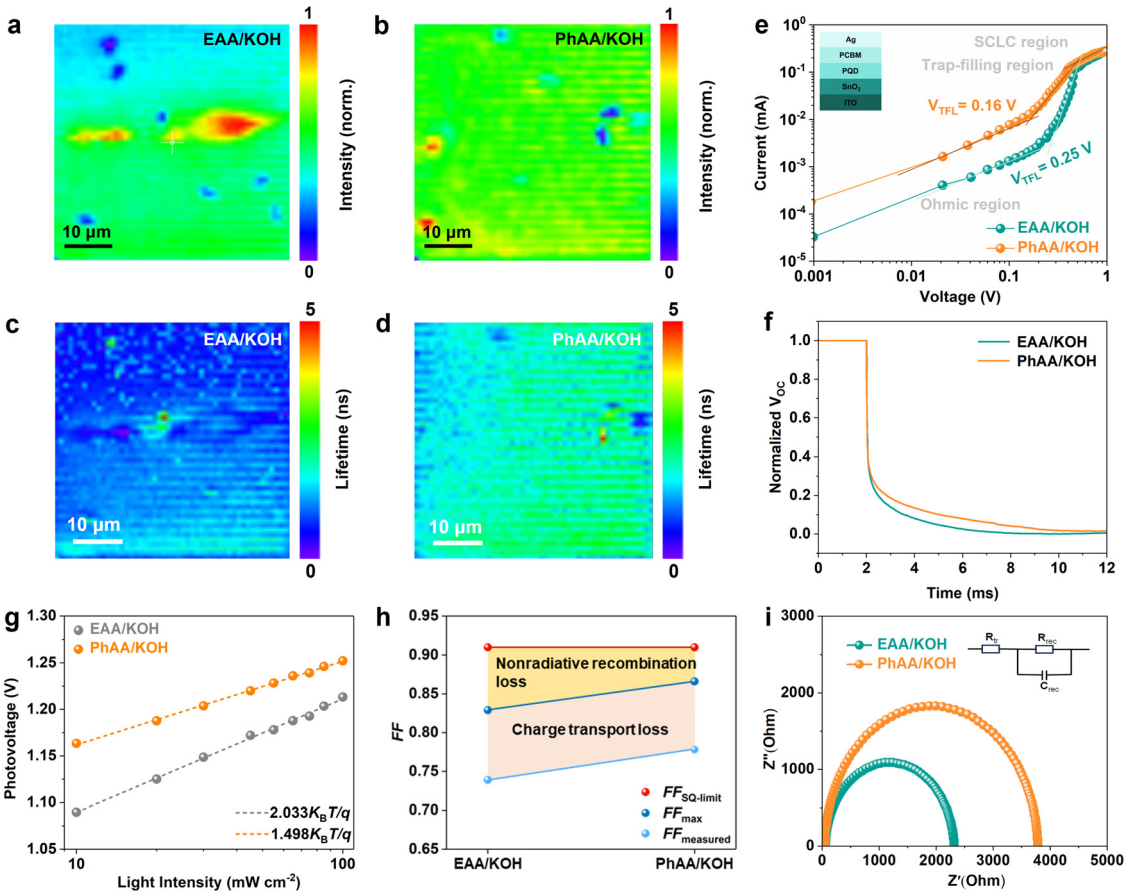


Fig. 4 Effects of the *in situ* NCR strategy on charge extraction and recombination dynamics. (a)–(d) Normalized 2D pseudo-color maps of PL intensity (a) and (b) and average fluorescence lifetime imaging microscopy (c) and (d) for EAA/KOH-based (a) and (c) and PhAA/KOH-based (b and d) PQD absorbers. (e) SCLC curves of EAA/KOH and PhAA/KOH electron-only devices. (f)–(i) TPV curves (f), light intensity-dependent V_{OC} plots (g), analysis of FF losses related to charge transport and nonradiative recombination (h), and Nyquist plots with the fitted equivalent circuit (i) for EAA/KOH and PhAA/KOH-based PQDSCs.

which exhibit a μ_e value of 3.44×10^{-4} cm^2 V^{-1} s^{-1}, PhAA/KOH-based devices show a markedly increased μ_e of 5.64×10^{-4} cm^2 V^{-1} s^{-1}. These improvements indicate that the *in situ* NCR strategy facilitates more efficient carrier extraction in the assembled PQD absorbers.

We next investigated charge carrier dynamics in complete PQDSC devices. Fig. 4f shows the transient photovoltage (TPV) curves, which were fitted with a bi-exponential decay function for analysis. PhAA/KOH-based PQDSCs exhibit a prolonged carrier lifetime of 2.76 ms compared with 1.54 ms for their EAA/KOH counterparts, suggesting suppressed charge recombination. To gain detailed insights, device performance was analyzed under varying light intensities. Light intensity-dependent J_{SC} measurements reveal that both PhAA/KOH- and EAA/KOH-based devices exhibit fitted exponential factors close to unity (Fig. S28a), confirming that bimolecular recombination dominates their operation process.[46] Light intensity-dependent V_{OC} (Fig. 4g) results were modeled by a linear function following eqn (5):

$$V_{OC} = \frac{n_{ID}kT}{q}\ln\left(\frac{J_{ph}}{J_0} + 1\right) \quad (5)$$

where k, T, J_{ph}, and J_0 are the Boltzmann constant, Kelvin temperature, photocurrent density, and reverse saturation current density, respectively. The slope of the linear relationship indicates that diode ideality factors (n_{ID}) decrease from 2.033 kT q^{-1} for EAA/KOH-based PQDSCs to 1.498 kT q^{-1} for PhAA/KOH-based devices, indicating suppressed Shockley–Read–Hall (SRH) recombination.[47]

We further examined nonradiative recombination and transport losses of photogenerated charge carriers to account for the improved FF values in PhAA/KOH-based devices. As shown in Fig. 4h, the maximum achievable FF without transport losses (FF_{max}) for PQDSCs was calculated using eqn (6) and (7):[48]

$$FF_{max} = \frac{\nu_{oc} - \ln(\nu_{oc} + 0.72)}{\nu_{oc} + 1} \quad (6)$$

$$\nu_{oc} = \frac{qV_{OC}}{n_{ID}k_BT} \quad (7)$$

Comparison of the FF_{max}, Shockley–Queisser limit FF ($FF_{S-Q\,limit}$) with the experimentally measured FF ($FF_{measure}$) reveals markedly reduced nonradiative recombination losses in the PhAA/KOH-based PQDSCs relative to their EAA/KOH

 This journal is © The Royal Society of Chemistry 2026

counterparts. This is consistent with their lower leakage current (Fig. S28b), confirming that the *in situ* NCR strategy substantially reduces trap-assisted carrier recombination in the fabricated PQDSCs. Moreover, electrochemical impedance spectroscopy (EIS) was employed to quantitatively characterize carrier recombination and transport behaviors in photovoltaic devices. Nyquist plots are shown in Fig. 4i, which were fitted with an equivalent circuit model. EAA/KOH-based devices show a recombination resistance (R_{rec}) of 2310 Ω and a charge transport resistance (R_{tr}) of 55.7 Ω. In comparison, PhAA/KOH-based PQDSCs exhibit a higher R_{rec} 3780 Ω with a lower R_{tr} of 45.2 Ω. These results demonstrate that the *in situ* NCR strategy simultaneously favors charge transport in PQD absorbers and suppresses charge recombination at device interfaces.

3. Conclusions

In summary, we have developed an *in situ* NCR strategy that effectively resolves the long-standing trade-off between ligand–exchange intensity and lattice stability in inorganic $CsPbI_3$ PQDs. Through synergistic optimization of acyl and alkoxy functionalities in ester molecules, PhAA was tailored as an accelerator for SSLE, whose acetoacetyl moieties, with doubled molar equivalents and higher coordination strength than conventional monoacyl groups, drive a 1.52-fold more complete substitution of pristine long-chain insulating oleate ligands with short conductive acetate species *via* efficient hydrolysis under alkaline conditions, thereby substantially strengthening inter-dot electronic coupling without inducing compositional leaching. Concurrently, the phenoxy groups of PhAA hydrolyze into low-polarity phenolic byproducts, which exhibit weaker adsorption and lower wetting on PQD surfaces compared to conventional alcohols. This feature effectively suppresses orthorhombic lattice distortion of the $CsPbI_3$ framework, thus favoring a uniform face-up crystallographic orientation in the resulting solid films. As a result, photovoltaic devices exhibit suppressed trap-assisted nonradiative recombination and enhanced charge extraction, delivering efficiencies of 17.66% and 14.86% for active areas of 0.07 and 1.00 cm^2, respectively, accompanied by a certified record efficiency of 17.07% for inorganic QDSCs. Moreover, these devices retain over 80% of their initial efficiency after 250 h of MPP tracking under the ISOS-L-1 protocol. This work establishes a molecular-level design principle for coordinating ligand–exchange chemistry and lattice integrity, providing a viable pathway toward high-performing and scalable quantum dot photovoltaics.

Author contributions

M. L., D. J., and J. L. conceived the idea and experimental projects. M. L., D. J., and Y. Z. guided the work as the supervisor. D. J., J. L., M. P., and X. W. were responsible for PQD synthesis and characterization. D. J., J. L., and K. Z. performed solar cell fabrication and photovoltaic measurements. Y. Z. performed PL mapping measurements. Z. L. conducted AFM tests. H. Q., P. C., and L. Z. participated in some photovoltaic measurements. D. J. and Y. H. conducted DFT calculations and data analysis. D. J. and J. L. wrote the first version of the manuscript and prepared figures. All authors contributed to discussions and commented on the manuscript, and all authors reviewed the manuscript.

Conflicts of interest

There are no conflicts to declare.

Data availability

The data supporting this article have been included as part of the supplementary information (SI). Supplementary information: including experimental sections and related measurements, including optical, electrical, and morphological properties *via* theoretical and experimental analysis, as well as device performance and parameters. See DOI: https://doi.org/10.1039/d6ee02756c.

Acknowledgements

This work is supported partially by the Beijing Natural Science Foundation (26JL001 and Z240024), the National Natural Science Foundation of China (52402255, 62404080, 52232008, 51972110, 52102245, and 62305111), the Fundamental Research Funds for the Central Universities (2024JC005), the Fundamental Research Funds for the Central Universities (2026MS056 and 2025MS039), the CHN Energy Investment Group under grant number GJNY-24-89 (S930024033), the NCEPU ''Double First-Class'' Program, and the Beijing Nova Program.

References

1 D. Jia, J. Chen, X. Mei, W. Fan, S. Luo, M. Yu, J. Liu and X. Zhang, *Energy Environ. Sci.*, 2021, **14**, 4599–4609.
2 A. Swarnkar, A. R. Marshall, E. M. Sanehira, B. D. Chernomordik, D. T. Moore, J. A. Christians, T. Chakrabarti and J. M. Luther, *Science*, 2016, **354**, 92–95.
3 L. M. Wheeler, E. M. Sanehira, A. R. Marshall, P. Schulz, M. Suri, N. C. Anderson, J. A. Christians, D. Nordlund, D. Sokaras, T. Kroll, S. P. Harvey, J. J. Berry, L. Y. Lin and J. M. Luther, *J. Am. Chem. Soc.*, 2018, **140**, 10504–10513.
4 J. Song, J. Li, X. Li, L. Xu, Y. Dong and H. Zeng, *Adv. Mater.*, 2015, **27**, 7162–7167.
5 G.-L. Yang and H.-Z. Zhong, *Chin. Chem. Lett.*, 2016, **27**, 1124–1130.
6 H. Huang, C. Zhao, X. Zhang, K. Wang, J. Fu, J. Guo, S. Wang, Q. Zhao, W. Ma and J. Yuan, *Nano Lett.*, 2023, **23**, 9143–9150.
7 H. Qiu, Y. Ji, W. Hu, F. Liu, D. Jia, L. Zhang, X. Lv and M. Li, *Nano Lett.*, 2025, **25**, 4393–4400.

8 P. Wu, Y. Liu, J. Yang, J. Hong, N. Song, J. He, Z. Guo and M. Liang, *Energy Mater.*, 2026, **6**, 600017.
9 Y. Ji, D. Jia, F. Xu, Z. Li, L. Zhang, L. Li and H. Qiu, *Chin. Chem. Lett.*, 2026, **37**, 112054.
10 D. Jia, J. Chen, R. Zhuang, Y. Hua and X. Zhang, *Energy Environ. Sci.*, 2022, **15**, 4201–4212.
11 D. Jia, J. Chen, M. Yu, J. Liu, E. M. J. Johansson, A. Hagfeldt and X. Zhang, *Small*, 2020, **16**, 2001772.
12 J. Hu, C. Bi, K. Ren, X. Zhang, W. Wang, S. Ma, M. Wei, Y. Lu and M. Sui, *Nano Lett.*, 2024, **24**, 4571–4579.
13 X. Ling, S. Zhou, J. Yuan, J. Shi, Y. Qian, B. W. Larson, Q. Zhao, C. Qin, F. Li, G. Shi, C. Stewart, J. Hu, X. Zhang, J. M. Luther, S. Duhm and W. Ma, *Adv. Energy Mater.*, 2019, **9**, 1900721.
14 D. Jia, J. Chen, J. Qiu, H. Ma, M. Yu, J. Liu and X. Zhang, *Joule*, 2022, **6**, 1632–1653.
15 H. Aqoma, S. H. Lee, I. F. Imran, J. H. Hwang, S. H. Lee and S. Y. Jang, *Nat. Energy*, 2024, **9**, 324–332.
16 L. Hu, Q. Zhao, S. Huang, J. Zheng, X. Guan, R. Patterson, J. Kim, L. Shi, C. H. Lin, Q. Lei, D. Chu, W. Tao, S. Cheong, R. D. Tilley, A. W. Y. Ho-Baillie, J. M. Luther, J. Yuan and T. Wu, *Nat. Commun.*, 2021, **12**, 466.
17 X. Zhang, H. Huang, X. Ling, J. Sun, X. Jiang, Y. Wang, D. Xue, L. Huang, L. Chi, J. Yuan and W. Ma, *Adv. Mater.*, 2021, **34**, 2105977.
18 H. Li, H. Huang, D. Li, X. Zhang, C. Zhao, X. Zhao, W. Ma and J. Yuan, *Energy Environ. Sci.*, 2025, **18**, 972–981.
19 L. Cao, Y. Tong, H. Wang and K. Wang, *Energy Mater.*, 2024, **4**, 400055.
20 E. M. Sanehira, A. R. Marshall, J. A. Christians, S. P. Harvey, P. N. Ciesielski, L. M. Wheeler, P. Schulz, L. Y. Lin, M. C. Beard and J. M. Luther, *Sci. Adv.*, 2017, **3**, eaao4204.
21 W. Travis, E. N. K. Glover, H. Bronstein, D. O. Scanlon and R. G. Palgrave, *Chem. Sci.*, 2016, **7**, 4548–4556.
22 H. Peng, D. Hou, J.-H. Guo, Y. Yu and W. Qin, *Chinese Chem. Lett.*, 2025, **37**, 111081.
23 G. Almeida, I. Infante and L. Manna, *Science*, 2019, **364**, 833–834.
24 D. Jia, J. Li, K. Zhu, H. Qiu, L. Li, X. Zhao, Z. Lan, H. Yan, F. Yang, P. Cui, X. Sun, H. Li, P. Zhu, S. Liu and M. Li, *Nat. Commun.*, 2025, **16**, 8612.
25 J. Ye, Z. Li, D. J. Kubicki, Y. Zhang, L. Dai, C. Otero-Martinez, M. A. Reus, R. Arul, K. R. Dudipala, Z. Andaji-Garmaroudi, Y. T. Huang, Z. Li, Z. Chen, P. Muller-Buschbaum, H. L. Yip, S. D. Stranks, C. P. Grey, J. J. Baumberg, N. C. Greenham, L. Polavarapu, A. Rao and R. L. Z. Hoye, *J. Am. Chem. Soc.*, 2022, **144**, 12102–12115.
26 J. Xue, J.-W. Lee, Z. Dai, R. Wang, S. Nuryyeva, M. E. Liao, S.-Y. Chang, L. Meng, D. Meng, P. Sun, O. Lin, M. S. Goorsky and Y. Yang, *Joule*, 2018, **2**, 1866–1878.
27 W. Yang, S. H. Jo, Y. Tang, J. Park, S. G. Ji, S. H. Cho, Y. Hong, D. H. Kim, J. Park, E. Yoon, H. Zhou, S. J. Woo, H. Kim, H. J. Yun, Y. S. Lee, J. Y. Kim, B. Hu and T. W. Lee, *Adv. Mater.*, 2023, **35**, 2304533.
28 J. Kim, S. Han, G. Lee, J. Choi, M. J. Ko and Y. Kim, *Chem. Eng. J.*, 2022, **448**, 137672.
29 X. L. Zhang, H. H. Huang, C. Y. Zhao, L. J. Jin, C. Lee, Y. Y. Li, D. H. Ko, W. L. Ma, T. Wu and J. Y. Yuan, *Nat. Energy*, 2024, **9**, 1378–1387.
30 J. Sun, S. Huang, X. Liu, Q. Xu, Q. Zhang, W. Jiang, D. Xue, J. C. Xu, J. Ma, J. Ding, Q. Ge, L. Gu, X. Fang, H. Zhong, J. Hu and L. Wan, *J. Am. Chem. Soc.*, 2018, **140**, 11705–11715.
31 K. Hoshi, T. Chiba, J. Sato, Y. Hayashi, Y. Takahashi, H. Ebe, S. Ohisa and J. Kido, *ACS Appl. Mater. Interfaces*, 2018, **10**, 24607–24612.
32 S. Shi, C. Gong, M. Tao, C. Wang, B. Fan, H. Yuan, H. Hu, M. B. K. Niazi, X. Yan, X. Hu and Y. Chen, *Nat. Synth.*, 2026, **5**, 209–220.
33 X. Li, F. Zhang, H. He, J. J. Berry, K. Zhu and T. Xu, *Nature*, 2020, **578**, 555–558.
34 R. An, F. Zhang, X. Zou, Y. Tang, M. Liang, I. Oshchapovskyy, Y. Liu, A. Honarfar, Y. Zhong, C. Li, H. Geng, J. Chen, S. E. Canton, T. Pullerits and K. Zheng, *ACS Appl. Mater. Interfaces*, 2018, **10**, 39222–39227.
35 J. Cui, Y. E. Panfil, S. Koley, D. Shamalia, N. Waiskopf, S. Remennik, I. Popov, M. Oded and U. Banin, *Nat. Commun.*, 2019, **10**, 5401.
36 S. Cho, J. Kim, S. M. Jeong, M. J. Ko, J.-S. Lee and Y. Kim, *Chem. Mater.*, 2020, **32**, 8808–8818.
37 B. Cheng, J. Yu, T. Arisawa, K. Hayashi, J. J. Richardson, Y. Shibuta and H. Ejima, *Nat. Commun.*, 2022, **13**, 1892.
38 M. A. Reus, A. Krifa, Q. A. Akkerman, A. Biewald, Z. Xu, D. P. Kosbahn, C. L. Weindl, J. Feldmann, A. Hartschuh and P. Müller-Buschbaum, *Adv. Opt. Mater.*, 2023, **12**, 2301008.
39 T. Dong, C. Shen, B. Yu, S. Zhao, H. Wu, C. Ding, B. Shi, Z. Cai, W. Hu, B. Shi, F. Ye, Q. Ye and Z. Fang, *Carbon Neutral*, 2025, **4**, 70061.
40 Q. Zhang, H. Huang, Y. Yang, M. Wang, S. Qu, Z. Lan, T. Jiang, Z. Wang, S. Du, Y. Lu, Y. Suo, P. Cui and M. Li, *Adv. Mater.*, 2024, **36**, 2410390.
41 W. Guo, J. Dai, S. He, L. Yang, Y. He, J. Duan, H. Cen, X. Yang, F. Yuan, J. Li, Z. Wu, L. Manna and J. Xi, *Adv. Sci.*, 2026, **13**, 20934.
42 Y. Wang, M. I. Dar, L. K. Ono, T. Zhang, M. Kan, Y. Li, L. Zhang, X. Wang, Y. Yang, X. Gao, Y. Qi, M. Gratzel and Y. Zhao, *Science*, 2019, **365**, 591–595.
43 D. W. deQuilettes, K. Frohna, D. Emin, T. Kirchartz, V. Bulovic, D. S. Ginger and S. D. Stranks, *Chem. Rev.*, 2019, **119**, 11007–11019.
44 Y. Yuan, G. Yan, C. Dreessen and T. Kirchartz, *Adv. Energy Mater.*, 2024, **15**, 2403279.
45 D. Jia, J. Chen, R. Zhuang, Y. Hua and X. Zhang, *Adv. Mater.*, 2023, **35**, 2212160.
46 C. Zhao, D. Li, X. Zhang, H. Huang, C. Cazorla, X. Zhao, H. Li, Y. Chen, W. Zhu, T. Wu and J. Yuan, *Adv. Mater.*, 2025, **37**, 12201.
47 D. Jia, J. Chen, S. Zheng, D. Phuyal, M. Yu, L. Tian, J. Liu, O. Karis, H. Rensmo, E. M. J. Johansson and X. Zhang, *Adv. Energy Mater.*, 2019, **9**, 1902809.
48 H. Huang, P. Cui, Y. Chen, L. Yan, X. Yue, S. Qu, X. Wang, S. Du, B. Liu, Q. Zhang, Z. Lan, Y. Yang, J. Ji, X. Zhao, Y. Li, X. Wang, X. Ding and M. Li, *Joule*, 2022, **6**, 2186–2202.

 This journal is © The Royal Society of Chemistry 2026